

Near-infrared line imaging of the circumnuclear starburst rings in the active galaxies NGC 1097 and NGC 6574

J.K. Kotilainen¹, J. Reunanen¹, S. Laine^{2,3}, S.D. Ryder^{4,5}

¹ Tuorla Observatory, University of Turku, Väisäläntie 20, FIN-21500 Piikkiö, Finland

² Department of Physical Sciences, University of Hertfordshire, College Lane, Hatfield, Herts. AL10 9AB, England, U.K.

³ Present address: Department of Physics and Astronomy, University of Kentucky, Lexington, KY 40506-0055, U.S.A

⁴ Joint Astronomy Centre, 660 N. A'Ohoku Place, Hilo, HI 96720, U.S.A

⁵ Present address: Anglo-Australian Observatory, P.O. Box 296, Epping, NSW 1710, Australia

Accepted; received

Abstract. We present high spatial resolution near-infrared broad-band JHK and $B\gamma 2.166 \mu\text{m}$ and $H_2 1-0\text{S}(1) 2.121 \mu\text{m}$ emission line images of the circumnuclear star formation rings in the LINER/Seyfert 1 galaxy NGC 1097 and in the Seyfert 2 galaxy NGC 6574. We investigate the morphology, extinction, and the star formation properties and history of the rings, by comparing the observed properties with an evolutionary population synthesis model.

The clumpy morphology in both galaxies varies strongly with wavelength, due to a combination of extinction, emission from hot dust and red supergiants, and the age of the stellar populations in the rings. The near-infrared and radio morphologies are in general agreement, although there are differences in the detailed morphology. From the comparison of $B\gamma$ and $H\alpha$ fluxes, we derive average extinctions toward the hot spots $A_V = 1.3$ for NGC 1097 and $A_V = 2.1$ for NGC 6574. The observed $H_2/B\gamma$ ratios indicate that in both rings the main excitation mechanism of the molecular gas is UV radiation from hot young stars, while shocks can contribute only in a few regions.

The starburst rings in both galaxies exhibit small $B\gamma$ equivalent widths. Assuming a constant star formation rate with $M_u = 100 M_\odot$ results in extremely long ages (up to 1 Gyr), in disagreement with the morphology and the radio spectral index of the galaxies. This situation is only slightly remedied by a reduced upper mass cutoff ($M_u = 30 M_\odot$). We prefer a model of an instantaneous burst of star formation with $M_u = 100 M_\odot$ occurring $\sim 6-7$ Myr ago. Gaseous nuclear bars parallel to the stellar nuclear bar were detected in both galaxies, and we derive $M \sim 100 M_\odot$ for the mass of the excited nuclear H_2 emission. Finally, we briefly discuss the connection between the rings, bars and the fuelling of nuclear activity.

Key words: Galaxies: individual: NGC 1097 – Galaxies: individual: NGC 6574 – Galaxies: Seyfert – Galaxies: starburst – Infrared: galaxies – Stars: formation

1. Introduction

Bright hot spots of star formation (SF) in the circumnuclear regions of spiral galaxies are often closely connected to the existence of a bar. In many cases, these hot spots make up a kpc-size ring or spiral pattern (e.g. Buta & Crocker 1993). Multiwavelength studies have shown that these starburst rings have high SF and supernova rates (e.g. Hummel, van der Hulst & Keel 1987, hereafter H87; Genzel et al. 1995).

The circumnuclear SF rings are thought to arise as a consequence of a bar-driven gas inflow and dynamical resonances in the bar (e.g. Combes & Gerin 1985; Friedli & Martinet 1993; Piner, Stone & Teuben 1995). Dense gas accumulates in shocked regions of orbit crowding along the leading edges of the bar, loses angular momentum and flows inward. The gas accumulates in a ring between the two inner Lindblad resonances (ILR) and experiences a starburst, either through collisions of molecular clouds or by gravitational collapse of the ring into dense fragments (e.g. Combes & Gerin 1985; Elmegreen 1994). If no ILRs exist, the gas may continue to flow inward, resulting in a nuclear starburst without a ring (Telesco, Dressel & Woltscroft 1993).

Although there are plenty of examples of nuclear ring galaxies without nuclear activity, suggesting that the nuclear rings and active galactic nuclei (AGN) are not necessarily intimately related, there is, however, an indicative statistical correlation between the existence of nuclear rings and AGN in barred galaxies (Knapen et al. 1999). One of the most important questions concerning the nuclear rings is, therefore, that of fuelling of the AGN in their centers. Since the large-scale flow slows down substantially at the ILR ring, additional mechanisms, such as

bar instability within a central gas disk ('bars within bars'; Shlosman, Frank & Begelman 1989), have been suggested to fuel the AGN.

Multiwavelength studies of AGN with circumnuclear rings can provide insights into how the massive star clusters in the rings and nuclear activity are related. The relatively unobscured near-infrared (NIR) emission provides a better handle than optical emission to quantify the properties of SF in galaxies. In this paper we present high resolution broad-band *JHK* images and the first NIR Br γ and H₂ 1–0 S(1) emission line images of two active galaxies with a circumnuclear SF ring, NGC 1097 and NGC 6574. Because of their brightness, large angular size and relatively face-on orientation, they provide excellent targets for studying these phenomena. Br γ originates from H II regions surrounding hot young OB star clusters, while H₂ arises from hot molecular gas and traces the material available for SF.

NGC 1097 is a nearby ($v_{sys} = 1275$ km s $^{-1}$; $D = 18.2$ Mpc; $1'' = 90$ pc; $H_0 = 70$ km s $^{-1}$ Mpc $^{-1}$) Sbb galaxy with a strong bar ($PA \simeq 141^\circ$), inclined at 46° (Storchi-Bergmann, Wilson & Baldwin 1996). Non-thermal emission due to shock compression of gas and dust associated with the smooth thin dust lanes at the leading edges of the bar is clearly visible in radio continuum (Ondrechen & van der Hulst 1983). NGC 1097 has an elliptical companion galaxy, NGC 1097A, which influences the western spiral arm by tidal interaction (e.g. Ondrechen, van der Hulst & Hummel 1989). NGC 1097 contains a nuclear stellar bar ($PA \simeq 28^\circ$; Quillen et al. 1995), almost perpendicular to the primary bar. Based on optical emission line ratios, the nucleus of NGC 1097 is usually classified as a LINER (Phillips et al. 1984) although the detection of broad, double peaked H α emission (Storchi-Bergmann et al. 1993) suggests a revised classification as a Seyfert 1.

The most intriguing feature of NGC 1097 is the bright, almost circular circumnuclear SF ring (diameter $\sim 18'' = 1.6$ kpc), which actually consists of two tightly wound clumpy spiral arms. It has been the target of extensive multiwavelength studies (e.g. H87; Gerin, Nakai & Combes 1987; Telesco et al. 1993; Barth et al. 1995; Quillen et al. 1995; Pérez-Olea & Colina 1996; Storchi-Bergmann et al. 1996). According to Storchi-Bergmann et al. (1996), the ring of NGC 1097 is situated between the two ILRs associated with the primary bar potential, in agreement with numerical simulations (Piner et al. 1995).

NGC 6574 is a little studied SABbc spiral galaxy at $v_{sys} = 2282$ km s $^{-1}$ ($D = 32.6$ Mpc; $1'' = 160$ pc). It is inclined at $\sim 40^\circ$ and is not strongly interacting with any other major galaxy, as evidenced by the symmetric rotation curve (Demoulin & Chan 1969). Its nucleus is classified as a Seyfert 2. Around the nucleus, there is an SF region consisting of spiral arms in the form of a wide pseudoring. This ring contains ~ 30 H α emission regions (González-Delgado et al. 1997).

This paper is arranged as follows. In Section 2 we discuss the observations, data reduction and the evolutionary model used. In Sections 3 and 4 we discuss the morphology of the circumnuclear rings, determine the extinctions to the SF complexes from comparison of the recombination line strengths, and constrain their SF properties, stellar populations and SF history by a detailed comparison among the NIR tracers and with the radio emission. We also discuss the origin of the H₂ emission in the ring. General discussion and conclusions are presented in Section 5.

2. Observations, data reduction and the evolutionary model

2.1. Observations

The observations of the Br γ 2.1661 μ m and H₂ 1–0 S(1) 2.121 μ m emission lines and the *JHK* bands were carried out in September 1998 with the 3.8 m United Kingdom Infrared Telescope (UKIRT) on Mauna Kea, Hawaii, under FWHM $0''.6$ – $0''.7$ seeing. We used the 256 \times 256 px IRCAM3 camera, with pixel size $0''.281$ px $^{-1}$ and field of view $\sim 70'' \times 70''$. For the emission line observations, we used cooled ($T = 77$ K) narrow-band filters and a Fabry–Perot (F–P) etalon with spectral resolution ~ 400 km s $^{-1}$ and equivalent width (EW) 0.0038 μ m.

For both emission lines, five 60 sec observations were made at each on-line (OL) wavelength and at the nearby blue (BC) and red (RC) continuum, shifted with respect to the line centre by $\sim \pm 1200$ km s $^{-1}$, following the sequence OL–BC–OL–RC and moving the telescope by $\sim 10''$ in a five point grid between the individual integrations for sky subtraction. This sequence was repeated until a sufficient on-line integration time was achieved. For the *JHK*-bands, five 30 sec integrations were made both centered on the galaxy and on sky 5' east. The total integration times for the *JHK*-bands and for the Br γ and H₂ emission lines are 150, 1800 and 2400 sec (NGC 1097) and 150, 2400 and 2400 sec (NGC 6574). Faint standard stars were observed in both broad-band and narrow-band filters immediately after the galaxy observations at similar airmass.

2.2. Data reduction

IRAF¹ was used to reduce the observations. The line images were divided by a flatfield made from linearized galaxy images, and sky-subtracted using the median of the five images at the same wavelength. These images were then aligned by using the nuclear position as reference, and merged into one on-line image and two continuum images. The alignment of the images is accurate to within a fraction of a pixel. Finally, the continuum images

¹ IRAF is distributed by the National Optical Astronomy Observatories, which are operated by the Association of Universities for Research in Astronomy, Inc., under cooperative agreement with the National Science Foundation.

were scaled with the continuum/line ratio measured from a standard star, combined, and subtracted from the on-line images, and the final line images were flux calibrated against the spectral type A standard stars HD 1160 ($M_K = 7.040$) and HD 201941 ($M_K = 6.626$). The reduction of the broad-band images consisted of linearization, flatfielding using a sky flat, and sky subtraction using the median of five sky images. UKIRT faint standard stars FS 29 and FS 35 were used to flux calibrate the broad-band images.

The sensitivity of the F-P is a function of both the line-of-sight (l.o.s.) velocity of the galaxy and the shift in the transmitted wavelength of the F-P over the field of view. These effects were corrected for by dividing the measured fluxes by an inverse Airy function (see e.g. Bland-Hawthorn 1995). For NGC 1097, a high resolution l.o.s. velocity field exists (Storchi-Bergmann et al. 1996). The only available l.o.s. velocity data for NGC 6574 were published by Demoulin & Chan (1969), who find the velocity to be constant to within 20 km s^{-1} at distances $6''$ – $18''$ from the nucleus, i.e. encompassing the ring. Therefore, we have assumed that the velocity depends only on the angle with respect to the line of nodes and the inclination. According to Demoulin & Chan (1969), the rotational amplitude is 240 km s^{-1} , inclination 40° and the position angle PA = 159° . Using these values, we have estimated the velocity field in the SF ring. In the nucleus, we assumed the l.o.s. rotational velocity to be 0 km s^{-1} .

The emission linewidths would also need to be considered. This would, however, require information about the line profiles in different parts of the rings, which is not available. However, usually the spectral lines are rather narrow, and this correction is likely to be small. In this paper, the emission line *images* have not been corrected for by the inverse Airy function, because then noise would depend on the position in the image. However, the observed emission line *fluxes* have been corrected for this effect. The observed line emission is weak, so to enhance the S/N, all images were smoothed to $1''$ resolution.

Photometry in all bands was performed at the location of the detected $\text{Br}\gamma$ emission regions. The aperture used for each region was selected to include as much as possible of the radiation, while avoiding overlap with neighbouring regions. The smallest distance between the nearest emission regions in these galaxies is $\sim 2''$, which is larger than the resolution of the smoothed images ($\sim 1''$) and much larger than the seeing during the observations ($\sim 0''.6$). The observed fluxes were corrected for Galactic extinction (de Vaucouleurs et al. 1991) and redshift (K-correction). We estimate a photometric accuracy in the *JHK* magnitudes of ~ 0.03 mag, in the *JHK* colours of ~ 0.05 mag, and in the emission line fluxes of $\sim 10\%$.

2.3. Extinction

Optical observations of starburst regions are much more hampered by the large and spatially variable extinction

than observations in the NIR ($A_K \sim 0.1 \text{ A}_V$). The derived extinction depends on the assumed geometry of the absorbing dust with respect to the emission region. In this paper we assume for the sake of simplicity and for easy comparison with previous determinations, the case of a foreground screen of dusty cloud filaments. The true dust distribution is, however, probably clumpy and mixed with the star clusters, resulting in a somewhat larger extinction. Therefore, the derived extinction values should be treated as approximations only. Note that the exact value of extinction does not affect the EWs of the emission lines, if the differential extinction between the lines and the continuum is small, as is usually the case in the NIR (Calzetti 1997 and references therein). Assuming standard interstellar dust properties, case B recombination (intrinsic $F_{\text{H}\alpha}/F_{\text{Br}\gamma} = 102$; Osterbrock 1989), and the Landini et al. (1984) interstellar extinction curve, $A_\lambda \propto \lambda^{-1.85}$, extinction towards the ionized sources can be determined from the observed $\text{Br}\gamma$ and $\text{H}\alpha$ fluxes.

This extinction strictly refers only to the ionized gas. The extinction experienced by the continuum can be estimated by comparing the observed broad-band colours of the emission regions to the average colours of normal unobscured spiral galaxies ($\langle J-H \rangle = 0.75$, $\langle H-K \rangle = 0.22$; Glass & Moorwood 1985). This method, however, may be biased toward low extinction regions, as the most heavily reddened regions may not be detectable in the *JHK* images. Also, the intrinsic colours of the galaxies may be bluer than in normal galaxies, leading to an underestimation of the continuum extinction.

2.4. The evolutionary Model

To interpret the SF properties, we have used the stellar population synthesis model of Leitherer et al. (1999; hereafter L99), which employs the latest stellar evolutionary tracks (e.g. Charbonnel et al. 1999) and stellar atmosphere models (e.g. Lejeune, Buser & Cuisinier 1997). It predicts the evolution of a large number of NIR, optical and UV spectral features as a function of the burst age, metallicity, and the initial mass function (IMF) with lower and upper mass cutoff and slope α , for the limiting cases of instantaneous burst of SF (ISF) and constant SF rate (CSFR).

The EW of $\text{Br}\gamma$, which is sensitive to the age of the starburst, was estimated by subtracting a de Vaucouleurs bulge model (depicting the old stellar population) from the *K*-band image and dividing the $\text{Br}\gamma$ fluxes with the remaining *K*-band fluxes. The L99 models predict the number of ionizing photons below 912 \AA , $N(\text{H}^0)$, which can also be estimated from the $\text{Br}\gamma$ flux as $N(\text{H}^0) [\text{s}^{-1}] = 7.63 \times 10^{13} L_{\text{Br}\gamma} [\text{erg s}^{-1}]$. $N(\text{H}^0)$ allows us to evaluate the mass of recently formed stars (in ISF) or the SF rate (SFR) via an assumed IMF (in CSFR). $N(\text{H}^0)$ can also be estimated from the thermal radio emission (Condon & Yin 1990): $N(\text{H}^0) = 7.1 \times 10^{49} D^2 \nu^{0.1} T_e^{-0.76} S_{\text{th}}$, where D is the distance in Mpc, ν is the frequency in GHz, T_e

is the electron temperature in 10^4 K and S_{th} is the thermal radio flux density in mJy. The supernova (SN) rate predicted by the L99 models can be compared with the rate derived from non-thermal radio emission (Condon & Yin 1990; based on Galactic SNe): $L_{NT} \sim 1.3 \times 10^{23} \nu^{-\alpha} v_{SN}$, where L_{NT} is the non-thermal radio luminosity in W Hz^{-1} , ν is the frequency in GHz, α is the spectral index of non-thermal radiation and v_{SN} is the SN rate in yr^{-1} .

Since we do not have enough data for more detailed modelling, and to allow an easy comparison with properties derived by previous authors, we assume solar metallicity, $\alpha = 2.35$, and consider two models in what follows: (1) ISF with $M_u = 100 M_\odot$ and (2) CSFR with $M_u = 30 M_\odot$. Note that our general conclusions remain unchanged if one uses other evolutionary models, e.g. those of Cervino & Mas-Hesse (1994) or Lancon & Rocca-Volmerange (1996). However, the exact age of the starburst strongly depends on the chosen burst duration and IMF.

3. Results

3.1. NGC 1097

3.1.1. Morphology

We have detected 14 emission regions at higher than 3σ level in the $\text{Br}\gamma$ emission line image of NGC 1097 (Fig. 1). There is quite good spatial correspondence between the brightest regions in the $\text{Br}\gamma$ and radio emission (H87; their Fig. 3). Because the non-thermal radio emission is believed to arise in SN remnants and the thermal radio emission to be reradiated UV emission from OB stars (e.g. Condon 1992), this correspondence is not surprising. The detailed differences between radio and $\text{Br}\gamma$ can be explained as a difference in the ages of the emitting regions, indicating several SF generations (see also e.g. NGC 7771, Reunanen et al. 1999). In the $J-K$ colour map (Fig. 2), the radio peaks correspond quite well to the reddest $J-K$ colours. The ring is considerably redder than its surrounding region. Possible explanations for this are emission from hot dust and red supergiants (RSG), or spatially variable extinction. The nucleus is also redder than the galaxy.

There is quite good spatial correlation between the $\text{H}\alpha$ (H87; their Fig. 5) and the $\text{Br}\gamma$ emission, indicating that the effect of extinction is not severe in NGC 1097 (see also Section 3.1.2). The worst correspondence is toward southeast of the nucleus. Based on radio and $\text{H}\alpha$, one would expect a $\text{Br}\gamma$ emission region between the regions 12 and 13, which is, however, not detected. This region has the largest F-P correction factors, and it is possible that a $\text{Br}\gamma$ emission region exists there, but such a large fraction of the emission is shifted outside the F-P filter that it remains below our detection limit.

The correspondence between the H_2 and the $\text{Br}\gamma$ emission (Fig. 1) is not as good as between $\text{H}\alpha$ and $\text{Br}\gamma$. The clearest difference is in the nucleus, which has strong resolved H_2 emission, but no detected $\text{Br}\gamma$ emission (see

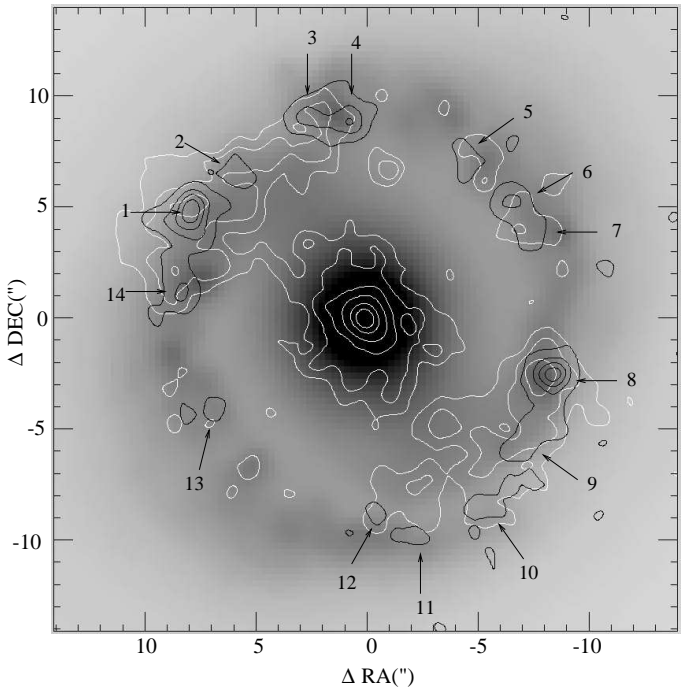


Fig. 1. The K -band image of NGC 1097, overlaid with the $\text{Br}\gamma$ emission (black contours) and the H_2 1–0 S(1) emission (white contours). The lowest contour is at 16 % level of the maximum and corresponds to 3σ . The other contours are at 40, 60 and 80 % ($\text{Br}\gamma$) and at 6.9, 12, 20, 35, 60 and 80 % (H_2) of the maximum. The maximum surface brightnesses are $1.1 \times 10^{-15} \text{ erg s}^{-1} \text{ cm}^{-2} \text{ arcsec}^{-2}$ for $\text{Br}\gamma$ and $1.7 \times 10^{-15} \text{ erg s}^{-1} \text{ cm}^{-2} \text{ arcsec}^{-2}$ for H_2 . In this and all subsequent figures, north is up and east to the left.

Section 3.1.3). We derive a nominal upper limit to the nuclear $\text{Br}\gamma$ emission of $1.5 \times 10^{-16} \text{ erg s}^{-1} \text{ cm}^{-2}$ in a $4''$ diameter aperture. In the circumnuclear region, the H_2 emission defines a broadly similar ring to $\text{Br}\gamma$, but there are differences in the detailed morphology.

Barth et al. (1995) observed NGC 1097 with the Hubble Space Telescope (HST) and resolved the hot spots in the ring into 88 star clusters. In Fig. 3 we show their V -band image overlaid in contours by our K -band image, and in Fig. 4, the $\text{Br}\gamma$ emission in contours is overlaid on the V -band image, which was Gaussian smoothed to the same resolution as $\text{Br}\gamma$. The effective radius of the brightest star clusters in the V -band, $R_{eff} = 3\text{--}7 \text{ pc}$, indicates that they represent individual SF regions. There is no perfect correlation between them and the $\text{Br}\gamma$ regions, although most $\text{Br}\gamma$ regions have a reasonably nearby V -band counterpart. There are differences especially in the north, where some $\text{Br}\gamma$ regions are situated in the V -band *minima*. Neither is there a perfect spatial correspondence between $\text{Br}\gamma$ and K -band (Fig. 1), although some $\text{Br}\gamma$ regions (e.g. region 8) have a clear counterpart in the K -

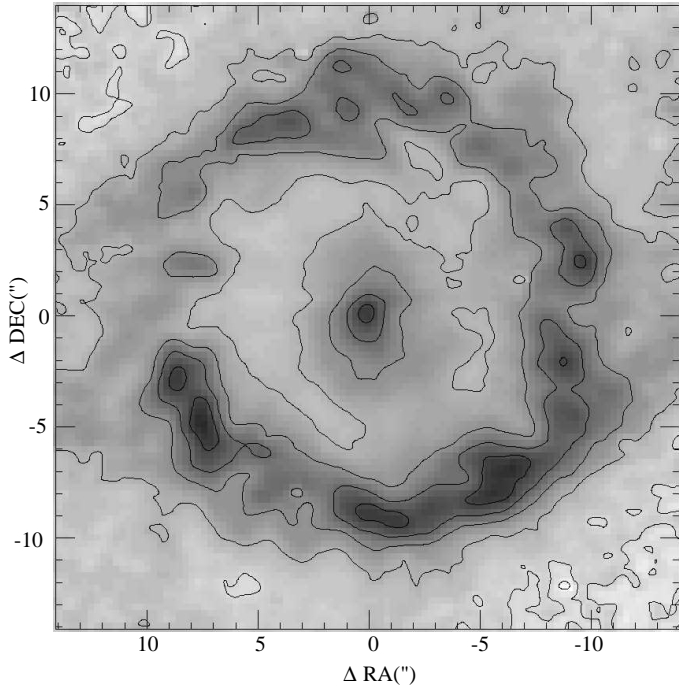


Fig. 2. The $J-K$ colour map of NGC 1097. The highest contour corresponds to $J-K = 1.4$ and the other contours are at $J-K = 0.1$ intervals.

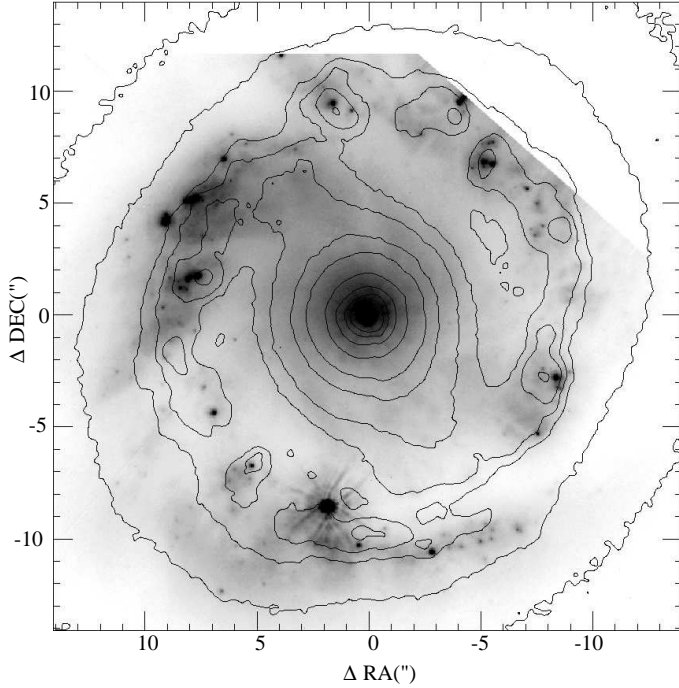


Fig. 3. The HST V -band image of NGC 1097 (Barth et al. 1995), overlaid in contours by the $0''.65$ resolution K -band image. The contours are at 2.5, 5, 10, 12.5, 15, 20, 35, 45, 55, 65 and 80 % of the K -band maximum. The strong point source $7''$ to the south of the nucleus is SN 1992bd.

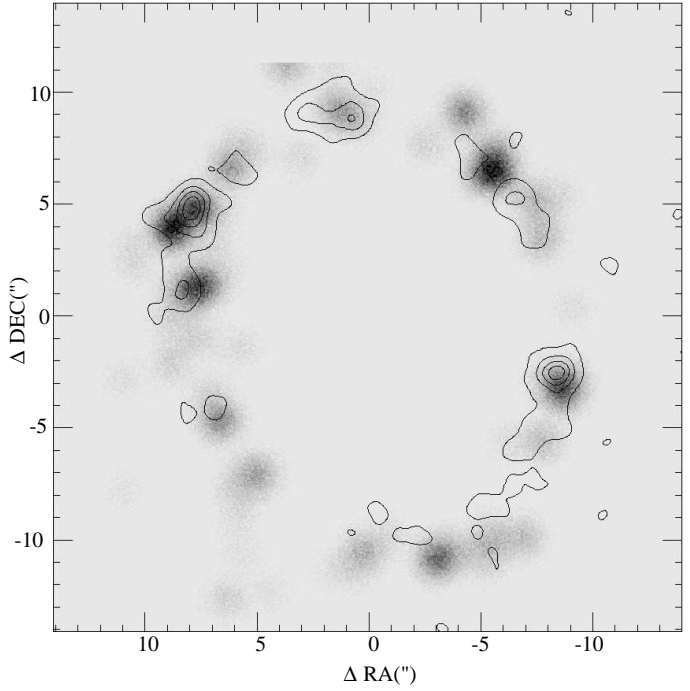


Fig. 4. The V -band HST image from Barth et al. (1995) overlaid in contours by the $Br\gamma$ image. The V -band image has been smoothed using a Gaussian FWHM corresponding to the width of the point source in the JHK and $Br\gamma$ images.

band. In many regions, however, there is overlap between the V - and K -bands and the $Br\gamma$.

The differences between $Br\gamma$, radio, V - and K -bands can be explained by differences in the age of the emission regions. The V -band peaks are probably younger than those in the K -band, since it takes 3–4 Myr before the emergence of the first RSGs that dominate the K -band emission. Less likely, the K -band peaks may either be regions of low extinction, or young dusty SNe.

3.1.2. Star formation properties

In Table 1 we give for the 14 $Br\gamma$ emission regions the aperture diameter in arcsec, the calibration coefficient from the Airy function, the $Br\gamma$ and H_2 fluxes, and the JHK colours. The smallest values of FWHM correspond to a size of the emitting region of $0''.8$ (70 pc). Therefore, the emission regions detected in the NIR actually are conglomerates of several OB associations and giant molecular clouds (c.f. $R_{eff} = 3 - 7$ pc; Barth et al. 1995), probably similar to scaled-up versions of the 30 Dor H II region in the LMC (e.g. Walborn et al. 1999).

Evans et al. (1996) gave for the $H\alpha$ emission regions in NGC 1097 the fluxes in instrumental units, but did not report the transformation coefficient into physical units. We have, therefore, calibrated the Evans et al. image using the lower resolution $H\alpha$ image (H87) which, however,

Table 1. Br γ emission regions in NGC 1097

n	ap	corr ^a	Observed emission				Br γ 10 $^{-15}$ ergs s $^{-1}$ cm $^{-2}$	H $_2$	J-H	H-K	Dereddened emission				
			Br γ 10 $^{-15}$ ergs s $^{-1}$ cm $^{-2}$	H $_2$	J-H	H-K					A V ^b	Br γ 10 $^{-15}$ ergs s $^{-1}$ cm $^{-2}$	H $_2$	$\frac{H_2}{Br\gamma}$	J-H
1	3.4	1.12	4.43	2.68	0.69	0.28	1.0	4.76	2.88	0.61	0.58	0.23			
2	2.0	1.01	0.68	0.72	0.70	0.26	1.1	0.74	0.78	1.05	0.58	0.20			
3	1.7	1.62	1.59	0.67	0.74	0.34	1.3	1.75	0.74	0.42	0.60	0.27			
4	1.7	1.69	1.87	0.46	0.72	0.37	1.3	2.06	0.50	0.25	0.59	0.30			
5	2.0	1.71	0.90	0.51	0.74	0.30	1.2	0.98	0.56	0.58	0.61	0.23			
6	1.4	1.75	1.05	0.34	0.72	0.30	1.5	1.31	0.37	0.32	0.57	0.22			
7	1.4	1.81	0.78	0.51	0.74	0.31	1.5	0.87	0.57	0.63	0.58	0.23			
8	3.4	1.17	2.96	2.68	0.79	0.32	1.8	3.39	3.06	0.91	0.61	0.22			
9	3.4	1.06	1.09	1.84	0.78	0.31	1.5	1.22	2.06	1.70	0.62	0.23			
10	3.4	1.06	0.85	1.16	0.79	0.33	1.2	0.93	1.27	1.36	0.66	0.27			
11	2.0	2.04	0.81	0.43	0.78	0.33	0.1	0.82	0.43	0.52	0.74	0.32			
12	2.0	1.98	0.71	0.73	0.81	0.37	0.3	0.73	0.75	1.04	0.76	0.35			
13	3.4	3.29	2.86	1.01	0.76	0.34	2.2	3.37	1.20	0.36	0.55	0.21			
14	3.4	1.79	3.57	2.74	0.70	0.27	2.2	4.21	3.24	0.77	0.48	0.15			
nucl	1.7	1.07	<0.15	2.68	0.84	0.34				>17.9					

^a: Correction factor for the velocity field and the change of wavelength across the array.

^b: Determined from the H α /Br γ ratio, assuming $A_\lambda \propto \lambda^{-1.85}$ (Landini et al. 1984).

partly includes upper limits. Following the method outlined in Section 2.3., we derive for the emission regions in NGC 1097 extinctions $A_V = 0.1\text{--}2.2$ (average $A_V = 1.3$). H87 derived, based on H α /H β , for the eastern (\sim region 1) and western (\sim region 8) parts of the ring extinctions $A_V = 0.85$ and $A_V = 2.83$, respectively. Other extinction determinations for NGC 1097 include average $A_V = 1.1$ for the ring (Barth et al. 1995), and $A_V = 0.6\text{--}3.0$ for various parts of the ring (Walsh et al. 1986). Our extinction determination is in good agreement with previous results, while the large spread between the emission regions indicates large spatial variation in the extinction within the ring. The extinction-corrected fluxes of the Br γ emission regions are given in Table 1.

The H $_2$ /Br γ ratio gives important clues about the excitation mechanism(s) of the hot molecular gas (Puxley, Hawarden & Mountain 1990). The main mechanisms suggested are thermal excitation in hot gas by low velocity shocks (e.g. Draine, Roberge & Dalgarno 1983) or by intense X-ray radiation (e.g. Maloney, Hollenbach & Tielens 1996), and fluorescent excitation by strong UV radiation (e.g. Black & van Dishoeck 1987). The observed H $_2$ /Br γ ratios for NGC 1097 (0.25–1.70, average 0.75) can mainly be explained with UV excitation by young stars (H $_2$ /Br $\gamma \simeq 0.4\text{--}0.9$; Puxley et al. 1990). In the regions where the ratio is larger than 0.9, the density of the gas clouds may be greater, the upper mass cutoff higher, or there may be a contribution from shock excitation, possibly due to supernovae. In fact, the regions with the largest H $_2$ /Br γ ratio (regions 2 and 9), are located at the opposite ends of the bar. This agrees well with the idea of a propagating starburst (e.g. Rieke et al. 1993), where SF

begins in the nucleus and propagates into the ends of the bar and into the circumnuclear ring through shocks in the bar. Further data, e.g. [FeII] 1.644 μm , are required to confirm the excitation mechanism(s).

We have determined the SF properties of NGC 1097 by comparing the observed quantities with the L99 models (Table 2). The Br γ EWs are small (8.1–30 \AA , average 15 \AA). Assuming the CSFR model with $M_u = 100 \text{ M}_\odot$, we derive very long ages for the burst, up to 1 Gyr, which are inconsistent with the clumpy K -band morphology of NGC 1097. During such a long time, these irregularities would have had time to smooth out. Also, the lifetime of individual giant molecular clouds in our Galaxy is only \sim 20–40 Myr, after which turbulence and heating from SNe disrupt them and inhibit further SF (Blitz 1991). Finally, gas consumption during such a long time with high mass SF would by far exceed the theoretical mass inflow rate into a circumnuclear ring (Piner et al. 1995). On the other hand, assuming a reduced upper limit to the mass function, $M_u = 30 \text{ M}_\odot$, we derive a much lower duration, 9.6–56 Myr, for the SF. The corresponding SFR is 0.05–0.31 $\text{M}_\odot \text{ yr}^{-1}$ (average $0.13 \text{ M}_\odot \text{ yr}^{-1}$, total within the ring $1.8 \text{ M}_\odot \text{ yr}^{-1}$) and SN rate is $0.5\text{--}2.2 \times 10^{-3} \text{ yr}^{-1}$ (average $1.0 \times 10^{-3} \text{ yr}^{-1}$, total within the ring $1.4 \times 10^{-2} \text{ yr}^{-1}$).

Assuming the ISF model, we derive even shorter ages, 6.2–6.7 Myr. The corresponding masses of the emission regions are $1.7\text{--}8.5 \times 10^6 \text{ M}_\odot$ (average $3.6 \times 10^6 \text{ M}_\odot$, total within the ring $5.1 \times 10^7 \text{ M}_\odot$) and the SN rate is $V_{SN} = 1.5\text{--}7.8 \times 10^{-3} \text{ yr}^{-1}$ (average $3.4 \times 10^{-3} \text{ yr}^{-1}$, total 4.7 $\times 10^{-2} \text{ yr}^{-1}$). The total mass of the hot gas, although large, is still only a small fraction of both the total stellar mass in the ring, $\sim 1 \times 10^9 \text{ M}_\odot$ (Quillen et al. 1995) and

Table 2. Star formation properties of NGC 1097

n	instantaneous star formation						constant star formation rate				
	$N(H^0)$ 10^{52} s^{-1}	EW Å	age Myr	mass $10^6 M_\odot$	SFR ^a $M_\odot \text{ yr}^{-1}$	v_{SN} 10^{-3} yr^{-1}	age	mass ^b $10^6 M_\odot$	SFR $M_\odot \text{ yr}^{-1}$	10^{-3} yr^{-1}	v_{SN}
1	2.82	30.3	6.23	6.56	0.95	6.4	9.56	3.0	0.31		1.0
2	0.44	8.5	6.63	1.74	0.26	1.6	49.2	2.3	0.05		1.0
3	1.04	19.8	6.36	3.06	0.48	2.9	11.4	1.3	0.11		0.6
4	1.22	20.2	6.35	3.53	0.56	3.3	11.3	1.5	0.13		0.6
5	0.58	11.7	6.53	2.08	0.32	1.8	24.9	1.6	0.07		0.9
6	0.78	18.9	6.37	2.33	0.37	2.2	11.7	1.0	0.09		0.5
7	0.52	12.3	6.51	1.82	0.28	1.6	22.6	1.3	0.06		0.7
8	2.01	16.8	6.40	6.39	1.00	6.0	12.8	2.8	0.22		1.3
9	0.72	8.1	6.65	2.99	0.45	2.8	56.2	4.4	0.08		1.5
10	0.55	8.1	6.65	2.29	0.34	2.1	56.2	3.4	0.06		1.1
11	0.49	10.6	6.57	1.79	0.27	1.6	30.0	1.6	0.05		0.8
12	0.43	12.1	6.52	1.72	0.26	1.5	23.3	1.1	0.05		0.6
13	2.00	19.8	6.36	5.89	0.93	5.6	11.4	2.5	0.22		1.1
14	2.50	14.3	6.46	8.51	1.32	7.8	16.0	4.4	0.28		2.2
total				51.0	7.8	47.0		32.2	1.8		10.0

^a: Mass divided by age^b: SFR multiplied by age

the total molecular gas mass, $M(H_2) = 1.3 \times 10^9 M_\odot$ (Gerin et al. 1987).

The reliability of conclusions based on *JHK* colours is reduced by our incomplete knowledge of the evolution and properties of RSGs (Origlia et al. 1999). The hot spots in the SF ring of NGC 1097 are much redder than their environment, although young stars ($t \sim 6$ Myr) should be blue. Only when the RSGs appear ($t \sim 10$ Myr), the colours become redder. Fig. 5 shows the *J*–*H* and *H*–*K* colour diagram of the $\text{Br}\gamma$ emission regions in NGC 1097, including the average *J*–*H* and *H*–*K* colours of normal unobscured spiral galaxies, and the effect of emission from hot dust at various temperatures. The extinction-corrected colours agree rather well with the L99 evolutionary model. The differences of the *H*–*K* colour with respect to the L99 model can be explained by assuming on average $\sim 20\%$ fractional contribution to the *K*-band emission from moderately hot dust. The *J*–*H* colour resembles the colour of a 8–9 Myr, not ~ 6 Myr, old ISF model. These ages, however, agree quite well, because the ISF model gives in fact a lower limit to the age of the burst, as the burst is not instantaneous, but it has a short, finite duration (shorter than the lifetime of the forming stars; $t <$ a few 10^6 yr). Furthermore, the NIR colours may be contaminated by older starburst generations.

Table 3 gives information about the radio emission in NGC 1097 (from H87), from which we have estimated the number of ionizing photons $N(H^0)$ and the SN rate v_{SN} . Most radio emission regions in NGC 1097 are dominated by non-thermal emission (on average 2/3 of the total). The total SN rate derived from the non-thermal radio emission is 0.053 yr^{-1} , which is in reasonable agreement

with the value derived from $\text{Br}\gamma$, 0.099 yr^{-1} . The latter value depends, however, on the adopted IMF parameters α and M_u . The $N(H^0)$ derived from the $\text{Br}\gamma$ emission is $\simeq 23 \times 10^{52} \text{ s}^{-1}$, whereas $N(H^0)$ derived from the thermal 4.885 GHz radio emission is $\simeq 43 \times 10^{52} \text{ s}^{-1}$. Note that an even larger difference between the $N(H^0)$ derived from radio and $\text{Br}\gamma$ was found for the starburst galaxy with a circumnuclear ring, NGC 7771 (Reunanen et al. 1999). For NGC 7771, we suggested that the fraction of the thermal radio emission had been overestimated, and the same may be applicable to NGC 1097.

The radio spectral index of NGC 1097 is between -0.46 and -0.97 within the ring (H87). According to the model of Mas-Hesse & Kunth (1991), the spectral indices observed for NGC 1097 are typical for an ISF of 5–9 Myr age. For the CSFR model, the steepest possible spectral index is ~ -0.25 . This strongly supports the conclusion that the ISF model is more likely to be applicable to NGC 1097. Further support for this comes from the clumpy *K*-band morphology (see above).

3.1.3. Nuclear emission

No $\text{Br}\gamma$ emission was detected in the nucleus of NGC 1097, suggesting that it does not contain large amounts of massive young stars. The nucleus, however, is a strong source of H_2 emission ($L(H_2) = 1.3 \times 10^5 L_\odot$ in $10''$ aperture), implying abundant fuel for SF. This is supported by the nuclear *JHK* colours, which are much redder than the colours of the bulge and resemble the colours of the ring. The simplest explanation for these colours is the presence of hot dust coexisting with the dense molecular gas.

Table 3. Radio emission of NGC 1097 (from Hummel et al. 1987)

n ^a	n ^b	S _{4.885GHz} mJy	α	S _{th} /S _{tot}	S _{th} mJy	v _{SN} 10 ⁻³ yr ⁻¹	N(H ⁰) ^c 10 ⁵²
1	3 4	5.36	-0.46	0.56	3.0	2.4	8.3
2 ^d	2	2.66	-0.58	0.37	1.1	1.7	2.7
3	1	3.34	-0.58	0.37	1.1	2.2	3.4
4 ^d	14	1.76	-0.97	—	—	1.8	—
5	13	5.36	-0.54	0.44	2.3	3.1	6.5
6	—	5.44	-0.62	0.30	1.5	3.9	4.6
7	12	3.86	-0.67	0.21	0.8	3.1	4.6
8	8	5.74	-0.53	0.45	2.6	3.3	7.1
9 ^d	—	2.66	-0.76	0.02	—	2.8	—
10	6 7	4.31	-0.51	0.48	2.3	2.3	5.7
	total					26.6	43

^a: Labeling by Hummel et al. (1987)

^b: The nearest Br γ emission region

^c: Determined assuming $T_e = 10^4 K$

^d: Between the 1.465 GHz radio emission regions

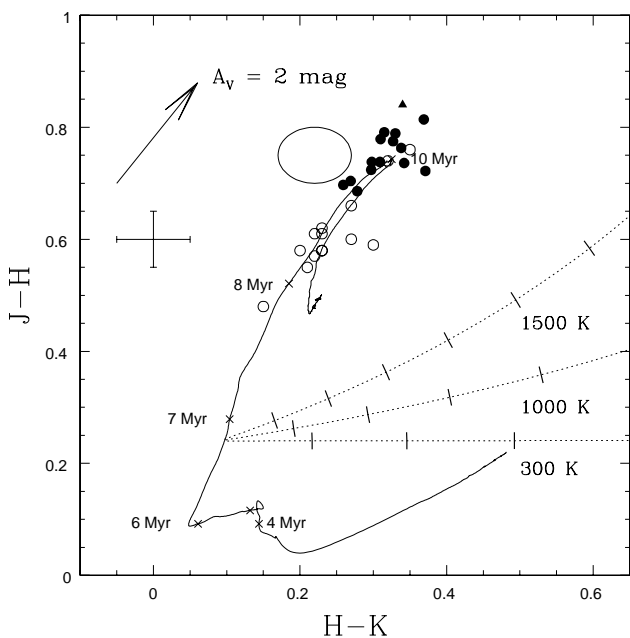


Fig. 5. The observed (filled circles) and extinction-corrected (open circles) $J-H$ and $H-K$ colours of NGC 1097. The nucleus is marked as a triangle. The ellipse shows the average colours of unobscured spiral galaxies (Glass & Moorwood 1985). The arrow shows the effect of extinction of $A_V = 2$ mag, and below the arrow are the photometric errors of the colours. The continuous line shows the L99 model colours for an instantaneous burst of star formation ($\alpha=2.35$, $M_u = 100 M_\odot$). The dashed lines show the effect of hot dust emission on the colours, with the tickmarks marking the fractional contribution of dust to the K -band emission at 10 % intervals.

The nuclear source of H₂ emission in NGC 1097 (Fig. 1) has a FWHM $0''.94$ (85 pc). Comparing this with the Gaussian FWHM resolution of the image ($0''.65$), we derive for the true extent of the resolved nuclear source $\sim 0''.7$ (65 pc). The PA of the resolved H₂ emission is $\sim 50^\circ$, whereas the PA of the stellar K -band bar is $\simeq 28^\circ$. Therefore, the H₂ emission is nearly elongated along but leading the stellar bar. Although kinematical data are required to verify its reality, the H₂ emission probably is in the form of a gaseous nuclear bar, and it appears that gas is flowing into the nucleus along the nuclear bar. Since the ellipticity of the isophotes is much larger in the H₂ than in the K -band, the gaseous H₂ bar is narrower than the stellar bar.

The average surface brightness of the nuclear H₂ emission in a $4''$ (360 pc) aperture is $2.1 \times 10^{-8} W \text{ cm}^{-2} \text{ sr}^{-1}$. Following the method of Meaburn et al. (1998), we derive $\sim 120 M_\odot$ for the mass of the excited H₂. This value should be multiplied by an unknown but probably small factor for the linewidth, which may be broader than the width of the F-P passband (see Section 2.2). The resulting mass, $M \sim 120 M_\odot$, is similar to those derived for the Seyfert galaxies NGC 3079 ($800 M_\odot$; Meaburn et al. 1998) and NGC 3227 ($250 M_\odot$; Fernandez et al. 1999). In all cases, the mass of the excited H₂ is only a small fraction of the available molecular gas mass.

Because the smallest Br γ EWs (oldest ages) are found near the ends of the nuclear bar, SF may have commenced in the nucleus (where it has already ended) and propagated into the ring through the nuclear bar. This possibility is also supported by the H₂/Br γ ratios in the ring, which indicate that shocks dominate the excitation of H₂ near the ends of the nuclear bar (Section 3.1.2). Similarly, the SN rate/SFR ratio is largest in the hot spots at the ends of the nuclear bar, suggesting that SF there

is decaying (i.e. fewer massive stars are produced, while the SN rate continues unchanged). Against the idea of a propagating starburst, we note that there is no strong evidence for recent star formation in the region between the nucleus and the ring either in Br γ (this work) or in radio and H α emission (H87). However, as studies of collisional ring galaxies (e.g. Appleton & Struck-Marcell 1996) and HI supershells (e.g. Ryder et al. 1995 and references therein) have shown, evidence of triggered bursts of massive star formation (e.g. X-rays or [S II] emission from SN remnants) can fade quickly.

Alternatively, the nuclear gaseous/stellar bar found in this study may be driving gas toward the nucleus to fuel the Seyfert. This is suggested by the models of e.g. Pfenninger & Norman (1990) and Friedli & Martinet (1993), in which the nuclear bar decouples from the primary bar and has a higher pattern speed. Such a short-lived ($\sim 10^8$ yr) nuclear bar would shock the circumnuclear gas at its leading edges, resulting in further gas inflow. The gaseous nuclear bar in NGC 1097 (and in NGC 6574, see Section 3.2.1) adds to the increasing number of such cases known in literature (e.g. NGC 3351, Devereux, Kenney & Young 1992; NGC 1808, Kotilainen et al. 1996; NGC 1068, Davies et al. 1998).

3.2. NGC 6574

3.2.1. Morphology

The K -band, Br γ and H $_2$ images of the nuclear region of NGC 6574 are shown in Fig. 6. We have detected 12 regions (including the nucleus) at higher than 3σ level in the Br γ emission. The spiral arms of NGC 6574 are clearly visible in the K -band, while the outer bar ($PA = 105^\circ$) can be seen in the $J-H$ colour map, but not in the $H-K$ map (Fig. 7). Fig. 8 shows the H α image (from González-Delgado et al. 1997), overlaid in contours with the Br γ image. Both the Br γ and H α emission regions are located in the spiral arms. Due to the higher S/N, H α emission regions are visible all along the spiral arms, whereas only the brightest Br γ regions can be seen. Many emission line regions have a counterpart in the K -band (Fig. 6), but the spatial correspondence is not perfect.

The morphology of the H $_2$ emission is different from that of Br γ (Fig. 6). East of the nucleus, near the end of the bar, there is the strongest region in both H $_2$ and Br γ , but the H $_2$ peak is closer to the nucleus. In northeast, Br γ is strong whereas H $_2$ is weak and diffuse. In the west, both emission lines are situated in the same regions, but H $_2$ is more broadly distributed. To the south of the nucleus there is neither H $_2$ nor Br γ emission, but this may be an artifact due to the narrow bandwidth of the F-P. The H $_2$ emission is elongated at the ends of the bar perpendicular to the bar. The nucleus is a strong source of H $_2$ emission ($L(H_2) = 4.6 \times 10^4 L_\odot$ in $10''$ aperture), but there is only weak Br γ emission. The FWHM of the nuclear H $_2$ source

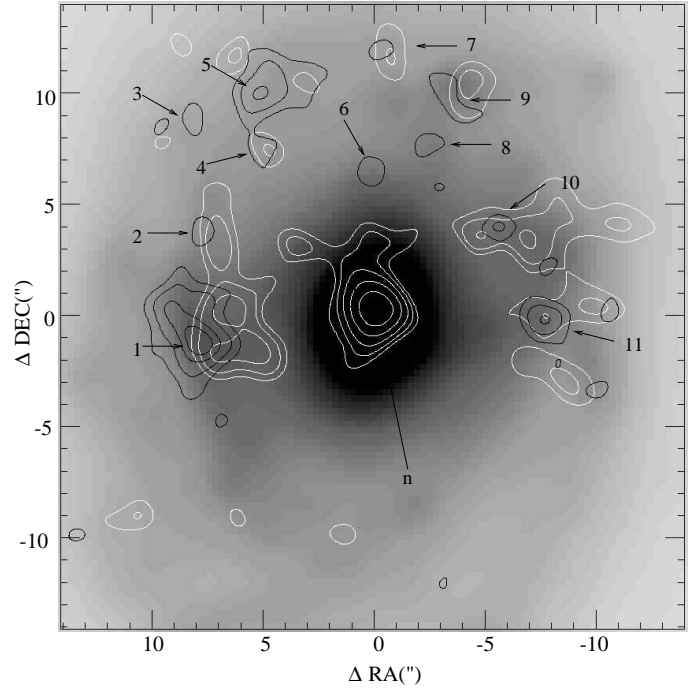


Fig. 6. The K -band image of NGC 6574 overlaid with Br γ (black contours) and H $_2$ 1–0 S(1) (white contours) emission. The Br γ and H $_2$ contours are at 31.5, 50, 70 and 85 %, and at 27.6, 35, 45, 60 and 85 % from the maximum level, respectively. The lowest contours are at 3σ level. The maximum surface brightnesses are 2.9×10^{-16} erg s $^{-1}$ cm $^{-2}$ arcsec $^{-2}$ for Br γ and 1.6×10^{-16} erg s $^{-1}$ cm $^{-2}$ arcsec $^{-2}$ for H $_2$.

is $\sim 1''.8$ (290 pc), much larger than the seeing FWHM $\sim 0''.7$. This resolved nuclear H $_2$ emission (Fig. 6) is closely parallel to but leading the nuclear stellar bar visible in the K -band ($PA \simeq 150^\circ$), and probably forms a gaseous nuclear bar. To the northwest and west of the nucleus there is an arc-like region of H $_2$ emission.

The average surface brightness of the nuclear H $_2$ emission in a $5''$ (800 pc) aperture is 2.6×10^{-9} W cm $^{-2}$ sr $^{-1}$. Following the method described in Section 3.1.2, we derive $\sim 80 M_\odot$ for the mass of the excited H $_2$, similar to that derived for NGC 1097 above.

We show the $J-H$ and $H-K$ colour maps of NGC 6574 in Fig. 7. Most, but not all, Br γ emission regions are situated close to the reddest colours. Both colour maps reveal the existence of a small spiral or bar structure around the nucleus. It is situated inside the spiral arms, but does not perfectly follow the morphology of the primary or nuclear stellar bar or the gaseous nuclear bar. In Fig. 9, we show the $J-K$ colour map, overlaid in black contours by the H $_2$ image. The H $_2$ emission follows the morphology in the $J-K$ colour map, and it is likely that the spiral/bar structure delineates the inflow route of the gas to the nucleus.

Table 4. Br γ emission regions in NGC 6574

n	ap "	corr ^a	Observed emission					Dereddened emission				
			Br γ 10^{-15} ergs s $^{-1}$ cm $^{-2}$	H $_2$ 10^{-15} ergs s $^{-1}$ cm $^{-2}$	J-H	H-K	A V ^b	Br γ 10^{-15} ergs s $^{-1}$ cm $^{-2}$	H $_2$ 10^{-15} ergs s $^{-1}$ cm $^{-2}$	$\frac{H_2}{Br\gamma}$	J-H	H-K
1	6.7	1.09	3.40	0.73	0.76	0.31	0.95	3.65	0.79	0.43	0.65	0.27
2	1.7	1.05	0.19	0.36	0.76	0.32	0.86	0.21	0.38	1.84	0.67	0.28
3	1.7	1.29	0.24	0.11	0.75	0.29	3.2	0.31	0.14	0.47	0.44	0.12
4	1.7	1.35	0.27	0.16	0.76	0.31	2.1	0.32	0.19	0.60	0.56	0.20
5	3.4	1.45	1.94	0.40	0.77	0.33	2.7	2.37	0.68	0.21	0.50	0.19
6	1.7	1.64	0.37	0.39	0.73	0.27	3.0	0.46	0.49	1.05	0.45	0.12
7	1.7	1.79	0.31	0.64	0.78	0.31	3.5	0.40	0.84	2.08	0.45	0.13
8	1.7	1.76	0.35	0.07	0.73	0.29	2.4	0.41	0.08	0.22	0.50	0.17
9	3.4	1.83	1.03	0.20	0.71	0.26	1.6	1.16	0.23	0.19	0.55	0.18
10	2.2	1.53	0.48	—	0.78	0.30	1.8	0.55	—	—	0.59	0.21
11	2.8	1.15	0.80	0.13	0.76	0.31	0.51	0.83	0.14	0.16	0.69	0.30
nucl	2.2	1.01	0.33	0.51	0.83	0.31	2.6	0.40	0.62	1.56	0.58	0.18

^a: Correction factor for the velocity field and the change of wavelength across the array.

^b: Determined from the H α /Br γ ratio.

3.2.2. Star formation properties

The observed results for the Br γ emission regions in NGC 6574 are given in Table 4. Note that the region marked with *nucl* is *close to* but not coincident with the nucleus. Using the H α image of NGC 6574 (González-Delgado et al. 1997) and the Br γ image, we derived extinctions of A V = 0.51–3.5 (average A V = 2.1) for the emission regions. To our knowledge, there are no previous determinations of extinction for the ring of NGC 6574. The observed fluxes of the emission regions were corrected for the extinction, resulting in values listed in Table 4.

The observed H $_2$ /Br γ ratios (0.16–2.1, average 0.73) are very similar to those found for NGC 1097 (Section 3.1.2). In most regions, the dominant excitation mechanism of the molecular gas is UV radiation from hot young stars (Puxley et al. 1990). Only in a few regions, the line ratio can be explained better by shocks.

The Br γ EWs of NGC 6574 are small (15–72 Å, average 35 Å). Although the EWs are slightly larger than in NGC 1097, even for NGC 6574 a CSFR model with M_u = 100 M $_{\odot}$ results in unreasonably large ages for the SF (up to 1 Gyr; Table 5). These ages are much smaller (7.9–15 Myr) assuming the CSFR model with a reduced upper limit of the mass function (M_u = 30 M $_{\odot}$). In this model, the SFR is 0.04–0.8 M $_{\odot}$ yr $^{-1}$ (average 0.21 M $_{\odot}$ yr $^{-1}$; total within the ring 2.3 M $_{\odot}$ yr $^{-1}$) and the SN rate is 0.2–3.3 $\times 10^{-3}$ yr $^{-1}$ (average 1.0 $\times 10^{-3}$ yr $^{-1}$; total within the ring 1.1 $\times 10^{-2}$ yr $^{-1}$). On the other hand, assuming an ISF model with M_u = 100 M $_{\odot}$, the derived ages are even lower with a small spread, 5.8–6.4 Myr, very similar to those found for NGC 1097. The small range of these ages supports preferring the ISF model, but an unambiguous separation of the models is not possible with the current data. Assuming the ISF model, we derive for the masses of the Br γ emission regions 1.2–19 $\times 10^6$ M $_{\odot}$ (aver-

age 4.2×10^6 M $_{\odot}$, total within the ring 4.6×10^7 M $_{\odot}$) and for the SN rate v_{SN} $1.1\text{--}19 \times 10^{-3}$ yr $^{-1}$ (average 4.0×10^{-3} yr $^{-1}$; total within the ring 4.4×10^{-2} yr $^{-1}$). Note that in Table 5, we do not list the values for the nucleus, since due to the weakness of the nuclear Br γ emission, we could not derive a realistic EW for it after the subtraction of the bulge model.

Fig. 10 shows the J-H and H-K colour diagram of the Br γ emission regions in NGC 6574. The observed J-H colours are similar to normal unobscured spiral galaxies, but the H-K colour is slightly redder, probably due to the contribution of hot dust emission. The extinction-corrected colours agree well with the L99 model but, as was found for NGC 1097, they indicate a slightly older population (7.5–8.5 Myr) than that derived from Br γ . A more physical model (e.g. a short duration or a decaying burst) would probably lead to a better agreement.

4. Discussion

We have studied two active galaxies with circumnuclear SF. NGC 1097 has a clear SF ring, the diameter of which, 1.6 kpc, is typical for the nuclear rings surrounding galactic nuclei (Buta & Crocker 1993). In NGC 6574, the Br γ emission regions are located in spiral arms, forming a pseudoring. The morphology of the galaxies changes with wavelength. There is a generally good, but not perfect, agreement between the K-band and the Br γ emission. The small differences probably reflect the existence of several SF episodes. Similarly, there is good but not perfect correlation between the H $_2$ and Br γ morphologies.

For both galaxies, we derived low Br γ EWs in the circumnuclear rings. Interpreting these values with a CSFR model and a high upper mass cutoff (M_u = 100 M $_{\odot}$) of the IMF leads to very old stellar population ages, up to 1

Table 5. Star formation properties of NGC 6574

n	instantaneous star formation						constant star formation rate				
	$N(H^0)$ 10^{52} s^{-1}	EW Å	age Myr	mass $10^6 M_\odot$	SFR ^a $M_\odot \text{ yr}^{-1}$	v_{SN} 10^{-3} yr^{-1}	age Myr	mass ^b $10^6 M_\odot$	SFR $M_\odot \text{ yr}^{-1}$	v_{SN} 10^{-3} yr^{-1}	
1	6.94	22.54	6.32	18.79	2.97	19.3	10.71	8.20	0.77	3.2	
2	0.39	14.81	6.44	1.31	0.20	1.2	15.02	0.64	0.04	0.3	
3	0.58	37.36	6.15	1.20	0.20	1.1	9.01	0.58	0.07	0.2	
4	0.60	30.91	6.22	1.37	0.22	1.3	9.51	0.63	0.07	0.2	
5	4.50	72.24	5.81	5.82	1.00	4.9	7.93	4.01	0.51	0.9	
6	0.88	28.04	6.26	2.14	0.34	2.1	9.82	0.96	0.10	3.3	
7	0.76	59.36	5.89	1.17	0.20	1.0	8.21	0.70	0.09	0.2	
8	0.79	27.66	6.26	1.92	0.31	1.9	9.87	0.86	0.09	0.3	
9	2.20	22.12	6.33	6.08	0.96	5.8	10.82	2.63	0.24	1.0	
10	1.04	35.21	6.18	2.24	0.36	2.1	9.15	1.06	0.12	0.4	
11	1.58	30.49	6.23	3.67	0.59	3.6	9.54	1.67	0.17	0.6	
total	20.3			45.7	7.4	44.3		21.9	2.3	10.6	

^a: Mass divided by age^b: SFR multiplied by age

Gyr. Reducing the upper mass cutoff in the CSFR model to $M_u = 30 M_\odot$ leads to more physically reasonable ages (9–50 Myr). The ISF model gives similar ages (6–7 Myr) for both galaxies, although there is a large scatter in the masses and SN rates of the emission regions. The small spread in the derived age both between the galaxies and within the emission regions is due to the very rapid decrease in the EW as a function of time in the L99 model at around 6–7 Myr, reflecting the fast evolution of the most massive stars away from the main sequence. It is possible that this similarity is a selection effect, as $\text{Br}\gamma$ can only reveal SF rings of a certain age. In NGC 1097, the observed radio spectral indices can not be explained in any CSFR model, so in this galaxy SF has already ended. A similar short duration ($t < 10^6 \text{ yr}$) SF episode has previously been suggested for e.g. the Seyfert 2 NGC 1068 (Davies et al. 1998), the starburst M82 (Rieke et al. 1993) and for the Galactic center (Genzel, Hollenbach & Townes 1994). Further support for the short ages comes from the NIR broad-band morphology. The K -band morphology of NGC 1097 is clumpy, indicating relatively young age as the irregularities have not yet had time to smooth out, and suggesting the presence of RSGs.

NGC 6574 has only a weak source of $\text{Br}\gamma$ emission in the nucleus, while no $\text{Br}\gamma$ was detected in the nucleus of NGC 1097. Either there is no SF in the nucleus, or it is too old to be detectable in $\text{Br}\gamma$. This situation agrees with the model of a propagating starburst, which has been suggested for e.g. Circinus (Maiolino et al. 1998), M82 (Satyapal et al. 1997) and IC 342 (Böker, Förster-Schreiber & Genzel 1997). In this model, SF has either commenced from the nucleus, and propagated into the ring through shocks in the bar, or it has started at the ends of the bar and propagated elsewhere into the ring. Both galaxies have strong resolved nuclear H_2 emission. It is thus also

conceivable that SF in the nucleus is prohibited and gas falls directly to the nucleus to fuel and obscure the AGN. Finally, a possible selection effect may explain the lack of observed SF in the nucleus, since if all rings are of roughly similar age, the nucleus may always be either too young or too old to produce a detectable amount of $\text{Br}\gamma$ emission.

The observed $\text{H}_2/\text{Br}\gamma$ ratios in both galaxies show a large spread. The dominant excitation mechanism of the gas appears to be UV radiation from hot young stars. The largest ratios in NGC 1097 are found at the ends of the bar, indicating a contribution from shock excitation and supporting the model of a propagating starburst.

The number of ionizing photons $N(\text{H}^0)$ derived for NGC 1097 from thermal radio emission is much larger than that derived from $\text{Br}\gamma$. This difference is unlikely to be caused by an incorrect determination of the radio spectral index, since the SN rate derived from non-thermal radio emission is in good agreement with that predicted by the L99 model. Either there exists thermal radio emission independently of SF, or the optical depth of $\text{Br}\gamma$ is large enough to allow the escape of only 10%–20% of the radiation from the emission regions. This would, however, indicate very large values of extinction A_V , which are not supported by the JHK colours.

Smith et al. (1999) proposed that the morphology of the circumnuclear ring reflects the mechanism which fuels the active nucleus. It is therefore instructive to compare the results found for NGC 1097 and NGC 6574 with other galaxies with circumnuclear rings with published $\text{Br}\gamma$ imaging. These include NGC 7771 (Reunanen et al. 1999), NGC 1808 (Kotilainen et al. 1996), NGC 7552 (Schinnerer et al. 1997), NGC 1068 (Davies et al. 1998) and NGC 7469 (Genzel et al. 1995). There is no strong correlation between the ring morphology and the strength of the nucleus. The circumnuclear morphology of NGC

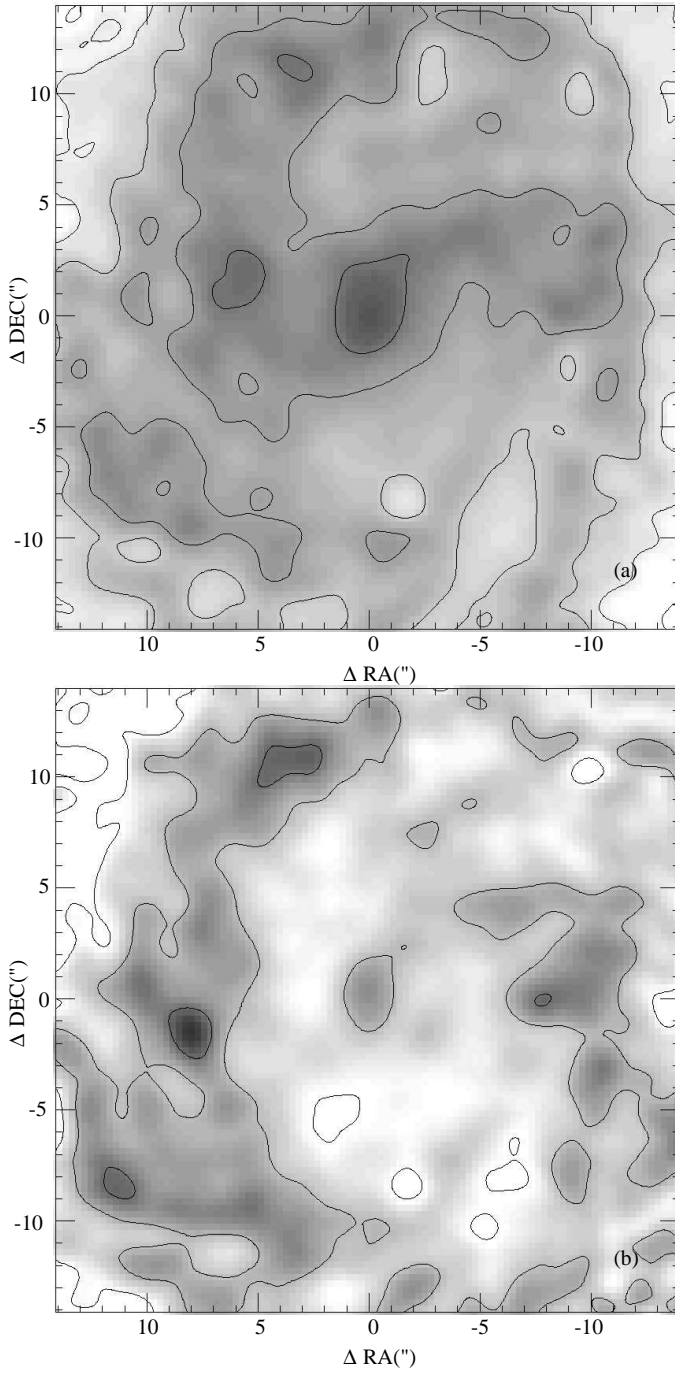


Fig. 7. The **a)** $J-H$ and **b)** $H-K$ colour maps of NGC 6574. The highest contours correspond to $J-H = 0.8$ and $H-K = 0.35$. The other contours are at $J-H = H-K = 0.05$ intervals.

7771 is much clumpier than that of NGC 7552, while neither contains an AGN, but a nuclear starburst. NGC 1808 has a nuclear starburst with a possible weak Seyfert, and its morphology is rather smooth. The circumnuclear ring of NGC 1097 with a weak Seyfert/LINER nucleus is very clumpy, while the rings in the strong Seyferts NGC 6574

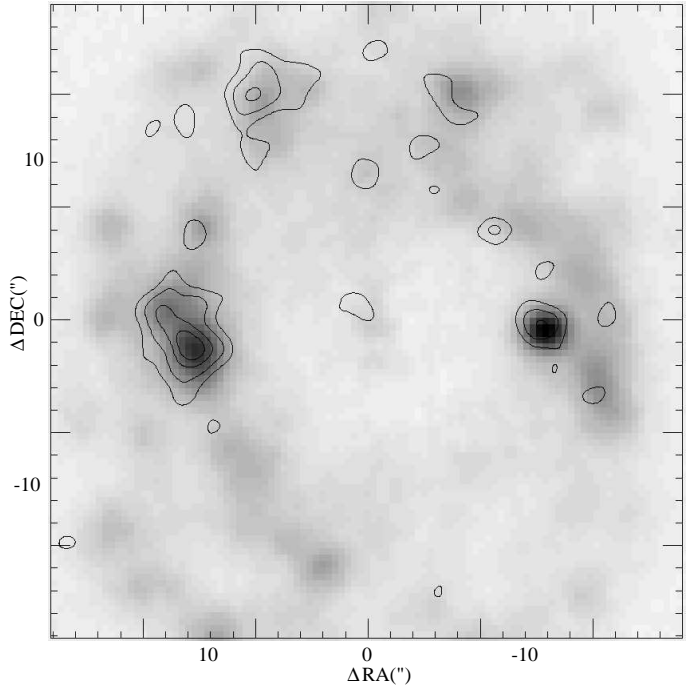


Fig. 8. The $H\alpha$ image of NGC 6574 (from González-Delgado et al. 1997), overlaid in contours by the $Br\gamma$ image.

and NGC 7469 are rather smooth. Finally, NGC 1068 with a strong Seyfert nucleus has a clumpy ring morphology.

A stronger inverse correlation is, on the other hand, found between the strength of the AGN and the strength of the bar. All three galaxies with a strong AGN (NGC 1068, NGC 6574 and NGC 7469) have a rather weak primary bar, whereas the four galaxies with a strong bar (NGC 1097, NGC 1808, NGC 7552 and NGC 7771) have either a weak or no AGN. This relationship agrees with the paucity of strong nuclear bars in AGN (Regan & Mulchaey 1999) and argues against the 'bars within bars' scenario (Shlosman et al. 1989) as the primary fuelling mechanism of nuclear activity. However, Seyfert galaxies have large-scale bars more often than non-active galaxies (Knapen et al. 1999), therefore a much larger sample of barred galaxies with circumnuclear rings is needed to study the implications of this correlation for the fuelling of AGN.

Acknowledgements. The United Kingdom Infrared Telescope is operated by the Joint Astronomy Centre on behalf of the U.K. Particle Physics and Astronomy Research Council. Thanks are due to Tom Geballe and Thor Wold for assistance during the observations, and to Rosa González-Delgado for kindly making the NGC 6574 $H\alpha$ image available to us. This research has made use of the NASA/IPAC Extragalactic Database (NED), which is operated by the Jet Propulsion Laboratory, California Institute of Technology, under contract with the National Aeronautics and Space Administration.

References

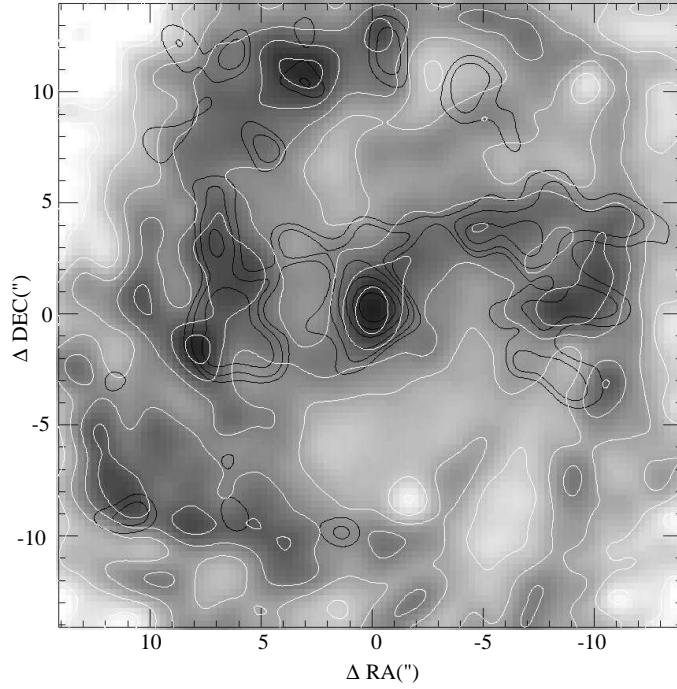


Fig. 9. The $J-K$ colour map of NGC 6574 highlighted in white contours. Overlaid in black contours is the H_2 1-0 S(1) image, with the lowest contour at 2.5σ level.

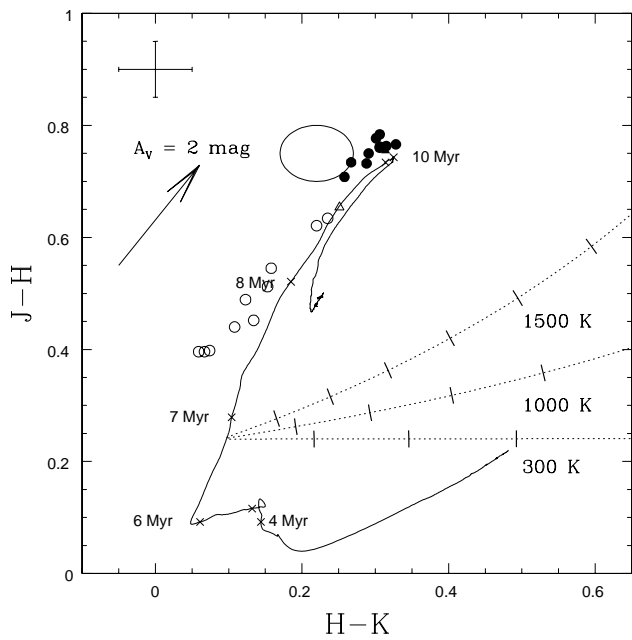


Fig. 10. As Fig. 5, but for NGC 6574.

Appleton P.N., Struck-Marcell C., 1996, Fund. Cosmic Phys. 16, 111
 Barth A.J., Ho L.C., Filippenko A.V., Sargent W.L.W., 1995, AJ 110, 1009
 Black J.H., van Dishoeck E.F., 1987, ApJ 322, 412

Bland-Hawthorn J., 1995, In: Comte G., Kylafis N. (eds.) ASP Conf. Ser. 71, Tridimensional optical spectroscopic methods in astrophysics, ASP, San Francisco, p. 72
 Blitz L., 1991, In: Lada C., Kylafis N. (eds.) ASI Series 342, The Physics of Star Formation and Early Stellar Evolution, Kluwer Academic Publishers, Dordrecht, p. 3
 Buta R., Crocker D.A., 1993, AJ 105, 1344
 Böker T., Förster-Schreiber N.M., Genzel R., 1997, AJ 114, 1883
 Calzetti D., 1997, AJ 113, 162
 Cervino M., Mas-Hesse J.M., 1994, A&A 284, 749
 Charbonnel C., Däppen W., Schaerer D. et al., 1999, A&AS 135, 405
 Combes F., Gerin M., 1985, A&A 150, 327
 Condon J.J., 1992, ARA&A 30, 575
 Condon J.J., Yin Q.F., 1990, ApJ 357, 97
 Davies R.I., Sugai H., Ward M.J., 1998, MNRAS 300, 388
 Demoulin M.-H., Chan Y., 1969, ApJ 156, 501
 de Vaucouleurs G., de Vaucouleurs A., Corwin H.G. et al., 1991, 3rd Reference Catalogue of Bright Galaxies, Springer-Verlag
 Devereux N.A., Kenney J.D., Young J.S., 1992, AJ 103, 784
 Draine B.T., Roberge W.G., Dalgarno A., 1983, ApJ 264, 485
 Elmegreen B.G., 1994, ApJ 425, L73
 Evans I.N., Koratkar A.P., Storchi-Bergmann T. et al., 1996, ApJS 105, 93
 Fernandez B.R., Holloway A.J., Meaburn J., Pedlar A., Mundell C.G., 1999, MNRAS 305, 319
 Friedli D., Martinet E., 1993, A&A 277, 27
 Genzel R., Hollenbach D., Townes C.H., 1994, Rep. Prog. Phys. 57, 417
 Genzel R., Weitzel L., Tacconi-Garman L.E. et al., 1995, ApJ 444, 129
 Gerin M., Nakai N., Combes F., 1987, A&A 203, 44
 Glass I.S., Moorwood A.F.M., 1985, MNRAS 241, 429
 González-Delgado R.M., Pérez E., Tadhunter C., Vilchez J.M., Rodríguez-Espinosa J.M., 1997, ApJS 108, 155
 Hummel E., van der Hulst J.M., Keel W.C., 1987, A&A 172, 32 (H87)
 Knapen J.H., Shlosman I., Peletier R.F., 1999, ApJ, in press (astro-ph/9907379)
 Kotilainen J.K., Forbes D.A., Moorwood A.F.M., van der Werf P.P., Ward M.J., 1996, A&A 313, 771
 Lancon A., Rocca-Volmerange B., 1996, New Astr. 1, 215
 Landini M., Natta A., Oliva E., Salinari P., Moorwood A.F.M., 1984, A&A 134, 284
 Leitherer C., Schaerer D., Goldader J. et al., 1999, ApJS 123, 3 (L99)
 Lejeune T., Buser R., Cuisinier F., 1997, A&AS 125, 229
 Maiolino R., Krabbe A., Thatte N., Genzel R., 1998, ApJ 493, 650
 Maloney P.R., Hollenbach D.J., Tielens A.G.G.M., 1996, ApJ 466, 561
 Mas-Hesse J.M., Kunth D., 1991, A&AS 88, 399

Meaburn J., Fernandez B.R., Holloway A.J., et al., 1998, MNRAS 295, L45

Ondrechen M.P., van der Hulst J.M., 1983, ApJ 269, L47

Ondrechen M.P., van der Hulst J.M., Hummel E., 1989, ApJ 342, 39

Origlia L., Goldader J.D., Leitherer C., Schaerer D., Oliva E., 1999, ApJ 514, 96

Osterbrock D.E., 1989, *Astrophysics of Gaseous Nebulae and Active Galactic Nuclei*, University Science Books

Pérez-Olea D., Colina L., 1996, ApJ 468, 191

Pfenniger D., Norman C., 1990, ApJ 363, 391

Phillips M.M., Pagel,B.E., Edmunds,M.G., Diaz,A., 1984, MNRAS 210, 701

Piner B.G., Stone J.M, Teuben P., 1995, ApJ 449, 508

Puxley P.J., Hawarden T.G., Mountain C.M., 1990, ApJ 364, 77

Quillen A.C., Frogel J.A., Kuchinski L.E., Terndrup D.M., 1995, AJ 110, 156

Regan M.W., Mulchaey J.S., 1999, AJ 117, 2676

Reunanen J., Kotilainen J.K., Laine S., Ryder S.D., 1999, ApJ, in press (astro-ph/9909140)

Rieke G.H., Loken K., Rieke M.J., Tamblyn P., 1993, ApJ 412, 99

Ryder S.D., Staveley-Smith L., Malin D., Walsh W., 1995, AJ 109, 1592

Satyapal S., Watson D.M., Pipher J.L. et al., 1997, ApJ 483, 148

Schinnerer E., Eckart A., Quirrenbach A. et al., 1997, ApJ 488, 174

Shlosman I., Frank J., Begelman M.C., 1989, Nat 338, 45

Smith D.A., Herter T., Haynes M.P., Neff S.G., 1999, ApJ 510, 669

Storchi-Bergmann T., Baldwin J., Wilson A.S., 1993, ApJ 410, L11

Storchi-Bergmann T., Wilson A.S., Baldwin J., 1996, ApJ 460, 252

Telesco C.M., Dressel L.L., Wolstencroft R.D., 1993, ApJ 414, 120

Walborn N.R., Barba R.H., Brandner W. et al., 1999, AJ 117, 225

Walsh J.R., Nandy K., Thompson G.I., Meaburn J., 1986, MNRAS 220, 453